On the mechanism of air entrainment by liquid jets at a free surface

By YONGGANG ZHU,† HASAN N. OĞUZ
AND ANDREA PROSPERETTI

Department of Mechanical Engineering, The Johns Hopkins University,
Baltimore, MD 21218, USA

The process by which a liquid jet falling into a liquid pool entrains air is studied experimentally and theoretically. It is shown that, provided the nozzle from which the jet issues is properly contoured, an undisturbed jet does not entrap air even at relatively high Reynolds numbers. When surface disturbances are generated on the jet by a rapid increase of the liquid flow rate, on the other hand, large air cavities are formed. Their collapse under the action of gravity causes the entrapment of bubbles in the liquid. This sequence of events is recorded with a CCD and a high-speed camera. A boundary-integral method is used to simulate the process numerically with results in good agreement with the observations. An unexpected finding is that the role of the jet is not simply that of conveying the disturbance to the pool surface. Rather, both the observed energy budget and the simulations imply the presence of a mechanism by which part of the jet energy is used in creating the cavity. A hypothesis on the nature of this mechanism is presented.

1. Introduction

Air entrainment occurs often in nature and is also encountered in many industrial operations. The pouring of liquids, breaking waves at the ocean surface, waterfalls, hydraulic jumps, are but a few examples of the many situations that are readily observed to cause the phenomenon. Air entrainment can be used to increase the surface area and thus the gas–liquid transfer efficiency in several chemical, fermentation and wastewater treatment processes. In fish farming, it is used to oxygenate the water particularly during the summer months or periods of intense fish activity. On the other hand, air entrainment may be undesirable, e.g. in the handling of molten glass and metals, plastics, cosmetics, paints or food products. For surface ships, air entrainment due to the bow wave and other waves around the hull can lead to propeller cavitation, underwater noise, and wakes that can be detected for many tens of kilometres.

In spite of this commonplace occurrence, the body of literature devoted to air entrainment is relatively small. One of the situations that has been studied the most – and that forms the object of the present paper – is air entrainment by liquid jets falling into a pool of the same liquid. Even in this relatively simple case our understanding of the process is however surprisingly poor. The detailed review of the work prior to 1993 given by Biń (1993), for example, shows discrepancies by factors of 3 or greater

† Present address: Advanced Fluid Dynamics Laboratory, CSIRO Division of Building, Construction and Engineering, Vic. 3190, Australia.

between different experiments. The numerous empirical correlations proposed in the literature are often in conflict with each other and with the data (see e.g. Detsch & Sharma 1990). Dimensionless parameters that collapse one investigator's data – e.g. the parameter X introduced by Van de Sande & Smith (1976) – do a very poor job when applied to other data sets such as those of Ohkawa, Kusabiraki & Sakai (1987), Funatsu, Hsu & Kamogawa (1988) or Kusabiraki *et al.* (1990). One may thus conclude that some basic physics is currently missing from our understanding of this seemingly simple process.

In an early but very important paper Lin & Donnelly (1966) made the exceedingly significant observation that, while for highly viscous laminar jets air entrainment is caused by the breakup of a quasi-steady air film enshrouding the jet below the liquid surface, for low-viscosity liquids, such as water, air entrainment is due to the surface roughness of the jet. This observation has been subsequently confirmed by several researchers such as Van de Sande & Smith (1976), Ervine, McKeogh & Elsawy (1980), McKeogh & Elsawy (1980), Sene (1988), and Bonetto & Lahey (1993), but the precise mechanism by which the process occurs has not been examined in detail. It is unclear how the disturbances on the jet surface trigger the entrainment and, once it is triggered, how much air is entrapped inside the pool. The effect of other parameters such as jet speed, turbulence level, nozzle geometry, viscosity of the liquid, etc. are also not well understood.

The objective of the present investigation is to probe the mechanism of air entrainment due to surface roughness. In order to avoid the randomness associated with turbulence generated by the nozzle, a single, well-characterized, and reproducible disturbance is generated on a smooth circular jet. In this way it is easier to study in detail the mechanics of entrainment. An unexpected finding of the present study is that a mechanism exists by which part of the kinetic energy of the jet is used by the surface disturbance to create the surface cavity that, upon collapse, results in air entrainment.

2. Experimental details

The experiments were carried out in a $0.75\,\text{m} \times 0.30\,\text{m} \times 0.30\,\text{m}$ laboratory tank (figure 1), in which the water level was kept constant by connecting it with a siphon to an overflowing smaller tank with adjustable water level. The vertical jet issues continuously from a nozzle with a nominal exit diameter D_j of 5.4 mm located $s = 55\,\text{mm}$ above the undisturbed water level. The nozzle consists of a linear expansion section, a settling chamber, and a contraction section. The shape of the contraction is especially designed to provide a very smooth flow at the exit. The jet velocity U_0 ranged from 0.96 to 1.87 m s^{-1} and was controlled by a rotameter (OMEGA FL 4503-V). The corresponding range of values for the Reynolds number $Re = U_0 D_j / v$ is 7100 to 14 000, for the Froude number

$$Fr = \frac{U_0^2}{gD_j}, \tag{2.1}$$

17.4 to 66, and for the Weber number

$$We = \frac{\rho U_0^2 D_j}{\sigma}, \tag{2.2}$$

68 to 260. Here v is the liquid kinematic viscosity, σ the surface tension coefficient, and g the acceleration due to gravity.
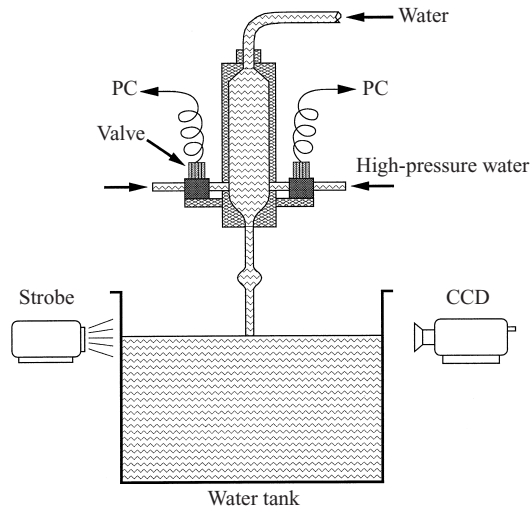
FIGURE 1. Experimental setup.

Case	P_{in} (kPa)	Q_{in} (ml s^{-1})	U_1/U_0	D_b/D_j
A	150	1.9	1.05	—
B	200	8.4	1.22	1.50
C	250	9.4	1.25	1.57
D	310	10.1	1.27	1.67
E	370	11.3	1.30	1.76
F	150	7.4	1.19	—

TABLE 1. Experimental conditions at $U_0 = 1.65$ m s^{-1}. $Re = 12300$, $Fr = 52$, $We = 202$.

Case	U_0 (m s^{-1})	U_1/U_0	D_b/D_j	h_b/D_j	Fr	We	Re
D1	1.87	1.24	1.65	—	66	260	13900
D2	1.65	1.27	1.76	—	52	202	12300
D3	1.32	1.33	2.19	0.65	33	129	9820
D4	0.96	1.46	2.25	0.68	17	68	7130

TABLE 2. Experimental conditions at $P_{in} = 310$ kPa gauge, $Q_{in} = 10.1$ ml s^{-1}.

The disturbance was generated by rapidly opening four computer-controlled solenoid valves that injected additional water from a pressurized reservoir through four side holes with a diameter of 3.2 mm in the contraction section of the nozzle 30 mm upstream of the exit. The pressure P_{in} in the reservoir was varied from about 140 to 400 kPa (gauge) to produce jet disturbances of different size. Two sets of experiments were carried out to investigate the effect of disturbance size and of the jet velocity. Details of these two sets of experiments are listed in tables 1 and 2. Here, U_0 and U_1 are the jet exit velocities before and after the opening of the solenoid valves, respectively. Q_{in} is the volumetric flow rate measured with the valves open in the absence of other flow. The parameters D_b and h_b characterize the size of the disturbance and are defined in § 3. In case A, only one valve was opened while in the other cases all four valves were opened.
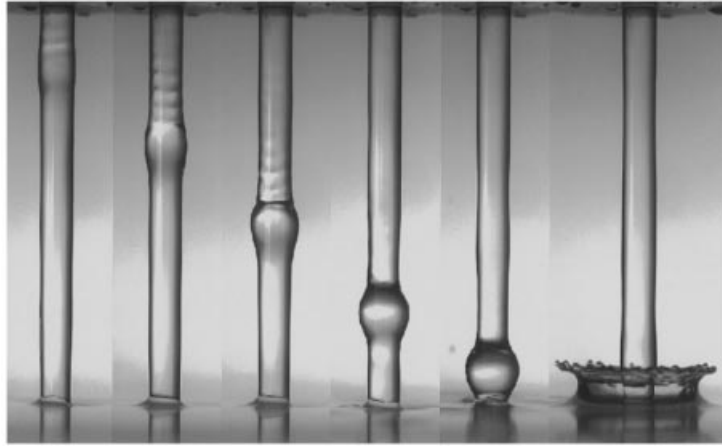
FIGURE 2. CCD images of the development of a jet disturbance between the nozzle and the receiving water surface (case C). Gravity points downward. The normalized times tU_0/D_j are, from left to right, 1.4, 3.2, 5.1, 6.9, 8.1 and 10.5, respectively. Here t is calculated from the time when the bulge appears at the nozzle exit.

A CCD camera (Pulnix TM-9701 with a Nikon lens) was used to capture 768×480-pixel images of the air entrainment process. Light was provided by a computer-controlled strobe. For each experimental condition, by suitably adjusting the time delay between water injection, strobe lighting, and camera exposure, a sequence of images of the jet and cavity at different stages of development was assembled. Since the event is highly reproducible, each sequence can be considered as depicting a single event. The images were stored in the computer for further processing. In some experiments, we also used a high-speed video or movie camera. For the latter, the computer provided suitable timing between water injection and the beginning of the filming. The film was then digitized and stored in the computer.

Edge-detection techniques were applied to the images to quantify several aspects of the process such as cavity and jet shape, depth and velocity of cavity, disturbance size, and speed of the jet. The resolution of the measurement was about ± 0.08 mm. The jet velocity was measured by means of tiny hydrogen bubbles ($50 \sim 100\,\mu$m) hydrolytically generated near the nozzle exit and convected by the jet. Images of these bubbles were captured using the CCD camera with a double exposure. The terminal velocity of the bubbles was too small (less than $5\,\text{mm}\,\text{s}^{-1}$) to have a significant effect on the velocity measurement. The photographic arrangement did not enable us to determine the radial position of the bubbles in the jet but one would not expect appreciable departures from a uniform velocity distribution over the jet cross-section in the conditions of the experiment.

3. Physical considerations

Figure 2 shows the development of the disturbance on the jet between the nozzle exit and the impact on the underlying water surface for case C of table 1. As noted before, even though each image refers to a different event, they can be considered as documenting the evolution of a single event in view of the high reproducibility of the experiment.

When the solenoid valves are opened, the flow rate out of the nozzle rapidly

increases. The faster-moving water catches up with the slower stream that has just left the nozzle and, essentially for kinematic reasons, a bulge forms on the jet surface. As more and more of the faster-moving water overtakes the slower-moving water, the bulge increases in size and evolves under the action of gravity and surface tension until it hits the pool liquid generating a thin splash (last frame of figure 2). A rather remarkable feature apparent from the photos is the nearly axisymmetric† upward curved meniscus that can be observed around the line of contact of the jet with the tank water prior to the impact of the disturbance.

The evolution of the pool liquid surface after the bulge strikes it is shown in detail in figure 3 for case C of table 1 and, in abbreviated form, in figure 4 for the other cases. The depth and width of the surface depression first increase as the kinetic energy of the bulge and of the jet is transformed into potential energy. After reaching a maximum size, the motion reverses and the rim of the cavity collapses against the jet at a certain depth below the undisturbed water level thus entrapping a toroidal bubble. The entrapped air with the severed jet inside continues to move downward before breaking up into smaller bubbles, while the remainder of the depression above the pinch-off point rises back toward the free surface. A similar sequence of events was observed in Oğuz, Prosperetti & Kolaini (1995), where the impact of a transient jet was studied. In that study it was shown that the depth at which the cavity closure occurs is dictated by a balance between the local hydrostatic pressure and the initial outward velocity imparted to the cavity wall.

The clarity of the reflection of the jet in the pool in all the frames of figure 2 except the last one indicates that, before the bulge hits the free surface, the pool water is not disturbed and indeed no entrainment occurs. The present observation is therefore in contradiction with several claims in the literature (e.g. that of Londong, quoted by Biń 1993) according to which air entrainment should occur if the Froude and Reynolds numbers exceed levels (10 and 7000, respectively, in Londong's case) that are amply exceeded in the present experiment without any observable entrainment. The point is that air entrainment is critically dependent on the presence of surface disturbances on the jet. Such disturbances are normally the result of turbulence, which is itself influenced by the details of nozzle design. Thus most of the critical values of the Reynolds number for air entrainment reported in the literature are really system-specific. They should be understood as quantifying at what value of Re jet surface disturbances sufficiently intense to entrain air appear in the authors' experimental setup. Furthermore, as figure 2 shows, surface disturbances evolve as they leave the nozzle. This remark explains why, in some studies such as Lara's (1979), a minimum jet length was found to be necessary for air entrainment at a fixed Reynolds number. Again, such observations must be used with caution as they are system-dependent.

From a superficial look at the sequence of events shown in figures 2 to 4, one might conclude that the kinetic energy of the bulge is converted into potential energy of the cavity. The underlying liquid jet would seem to play only the relatively passive role of 'guiding' the bulge from the nozzle to the surface of the pool liquid. A closer analysis (substantiated by the numerical simulations described in §6) shows however that this interpretation is untenable and that some subtle mechanism is actually involved here. Indeed, for example for the case of figures 2 and 3, the kinetic energy of the bulge just before entering the pool is about 0.5 mJ, while the gravitational potential energy stored in the cavity at its maximum volume, excluding any residual kinetic energy of the surrounding water and the energy carried away by surface waves, is about 0.8 mJ.

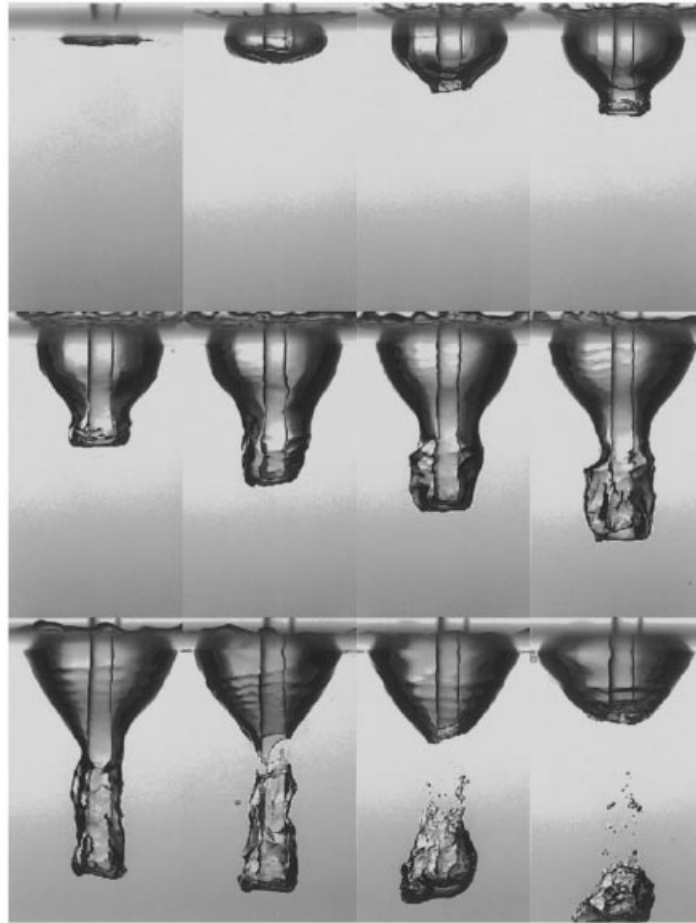† Deviations from axial symmetry are most likely due to slight disturbances on the pool surface.

FIGURE 3. CCD images of an underwater air cavity induced by the jet disturbance (case C). The dimensionless times tU_0/D_j, measured from the time when the bulge appears at the nozzle exit, are, from left to right: top row: 9.0, 10.2, 11.4 and 12.7; middle row: 13.9, 15.7, 17.0 and 18.2; bottom row: 19.4, 20.0, 20.9 and 22.2. The flow conditions are the same as in figure 2.

Thus, although the cavity is initiated by the bulge, there is a mechanism at work by which part of the jet energy also contributes to its formation. We now turn to a description of this mechanism.

3.1. *Role of the jet energy*

A useful starting point to explain the mechanics of the process under consideration is the observation that the cavity depicted in figures 3 and 4 clearly consists of two parts: an upper, relatively broad and shallow depression, and a thinner, deeper hollow that extends below the bottom of the upper depression. These two features correspond to different stages of the process and are the result of different physical mechanisms. The first stage – the formation of the upper depression – is similar to that encountered upon the impact of drops and other liquid masses on liquid surfaces (Oğuz & Prosperetti 1990; Oğuz *et al.* 1995) and, as will be shown shortly, can be entirely imputed to the impact of the bulge. The second stage of the process is the
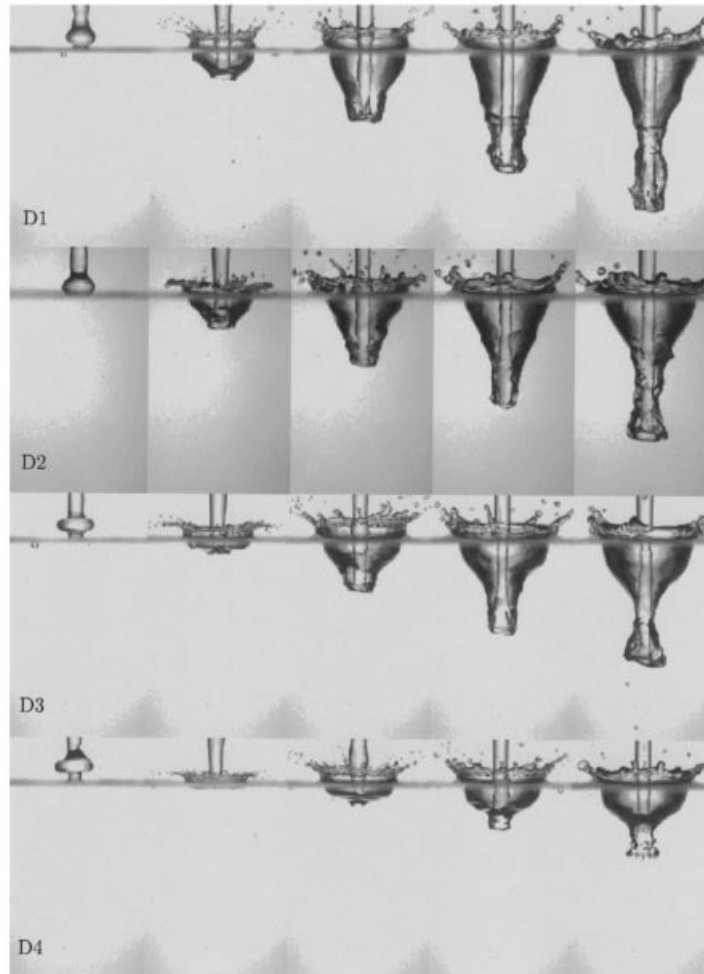
FIGURE 4. CCD images of underwater air cavities induced by the jet disturbance at four different jet velocities: $1.87\,\mathrm{m\,s^{-1}}$ (case D1, top row), $1.65\,\mathrm{m\,s^{-1}}$ (case D2, second row), $1.32\,\mathrm{m\,s^{-1}}$ (case D3, third row) and $0.96\,\mathrm{m\,s^{-1}}$ (case D4, bottom row). The times tU_0/D_j for the five images in each row are, from left to right: (D1) -0.3, 3.1, 6.5, 13.4, 16.2; (D2) 0, 3.1, 5.5, 8.0, 10.4; (D3) -0.5, 1.5, 3.9, 6.4, 8.3; (D4) -0.4, 0.7, 1.8, 3.0, 4.6. Here t is calculated from the time when the bulge hits the pool surface.
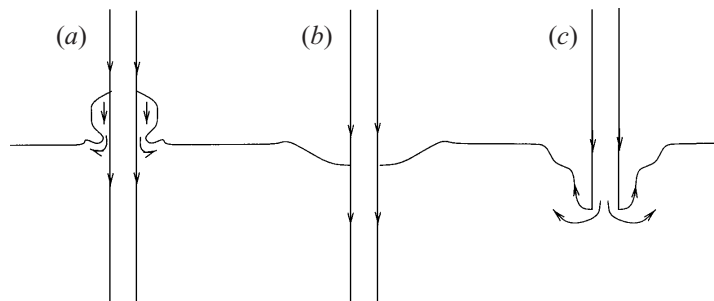

FIGURE 5. Sketches of the flow (*a*) at the moment of the bulge impact, (*b*) in the early stages after the impact, and (*c*) after reattachment of the streamlines.
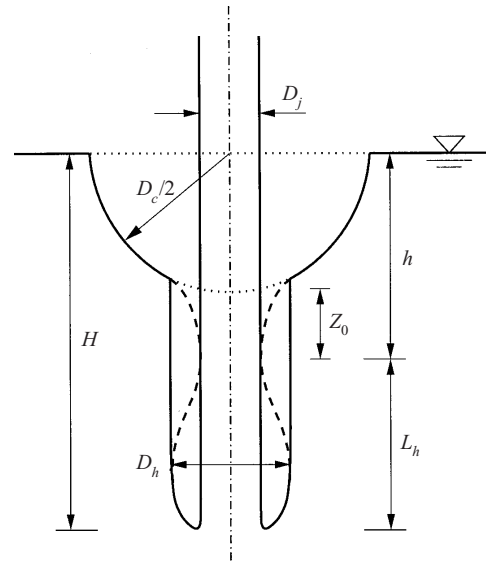
FIGURE 6. Definition of the geometric parameters of the underwater cavity.

penetration of the jet through the bottom of the depression produced by the bulge impact. This process requires a radical qualitative modification of the nature of the flow as shown in figure 5. Part (*b*) of the figure illustrates the flow regime prevailing in figure 2 and the initial stages of the bulge impact, while part (*c*) shows the flow that is necessary for the generation of the deeper hollow. In this flow the streamlines on the jet surface do not separate from the pool surface, as in part (*b*), but flow along it. The change in the momentum of the jet fluid exerts a downward force on the pool surface that generates the hollow. The transition between the two flow patterns requires a deflection of the jet streamlines that forces them to reattach to the pool surface. It seems reasonable to identify the high pressure caused by the bulge impact as the agent of this deflection.

We now proceed to make these considerations more quantitative, beginning from the first stage. As shown in Oğuz & Prosperetti (1990), one can get an estimate of the depth of the initial depression by equating the kinetic energy of the impacting liquid mass to the gravitational potential energy stored in it. If the volume of the bulge (with the exclusion of the portion of jet inside it) is V, and if the depression is approximated as a hemisphere of diameter D_c (see figure 6), we have

$$\tfrac{1}{2} V U_b^2 \simeq \tfrac{1}{12} \pi D_c^3 g \left(\tfrac{3}{16} D_c \right), \tag{3.1}$$

where U_b is the velocity of the liquid in the bulge and the last term in parentheses is the depth of the centre of mass of the hemispherical depression. In terms of the Froude number (2.1) this equation gives

$$\frac{D_c}{D_j} = 2 \left(\frac{2V}{\pi D_j^3} \frac{U_b^2}{U_0^2} Fr \right)^{1/4}. \tag{3.2}$$

The approximation $U_b \simeq U_0$ introduces at most an error of a few percent for the present experimental conditions. If the bulge is approximated as a cylinder coaxial

with the jet having a diameter D_b and a height h_b, the volume of the fluid it contains is

$$\frac{2V}{\pi D_j^3} = \frac{1}{2}\left(\frac{D_b^2}{D_j^2} - 1\right)\frac{h_b}{D_j}, \tag{3.3}$$

while, if we take it to be a sphere of diameter D_b, the corresponding result is

$$\frac{2V}{\pi D_j^3} = \frac{1}{2}\left(\frac{D_b^2}{D_j^2} - 1\right)^{1/2} + \frac{1}{6}\left[\frac{D_b}{D_j} - \left(\frac{D_b^2}{D_j^2} - 1\right)^{1/2}\right]^2\left[2\frac{D_b}{D_j} - \left(\frac{D_b^2}{D_j^2} - 1\right)^{1/2}\right]. \tag{3.4}$$

In either case, with the typical values of D_b and h_b appropriate for our experiment, we find

$$\frac{D_c}{D_j} \simeq 2c(Fr)^{1/4}, \tag{3.5}$$

where c is a constant of order 1. For a typical case $D_b/D_j = 1.5$, $2V/\pi D_j^3 = 0.6$ and c is about 0.9. This relation tends to overestimate the measured depression diameter with a maximum error of the order of 18%. This is not surprising as, in formulating the energy balance (3.1), we have assumed that there is no residual kinetic energy in the liquid and neglected the energy radiated away in the form of surface waves. The important point is, however, that (3.2) does give a reasonable estimate of the depression diameter.

And now let us turn to the second stage. During liquid–liquid impact a high pressure prevails in the stagnation region. This is the reason why, for example, the liquid of a drop falling on a free surface is deflected to flow along the surface itself (see e.g. Worthington 1908; Prosperetti & Oğuz 1993). For the same reason, the initial impact of a jet on a liquid surface generates a depression because the high stagnation pressure causes the streamlines to follow the free surface. If the flow remained potential, this pattern would persist, in agreement with classical analyses, e.g. of the penetration of shape charges (see e.g. Richardson 1948; Gilbarg & Anderson 1948; Birkhoff & Zarantonello 1957). In practice, however, the strong curvature of the flow causes a transition to a regime in which the jet streamlines detach from the free surface and penetrate the underlying liquid as an annular shear layer. This is the steady regime of flow of figure 2. To render plausible the hypothesis that the stagnation pressure generated by the bulge impact is capable of deflecting the jet streamlines forcing them to reattach to the pool surface, we recall some earlier results (Oğuz *et al.* 1995). In that paper we studied the impact of a jet on a free surface and we showed, on the basis of a simplified model, that the diameter D_h of the hollow produced by the jet is related to the jet diameter by the relation†

$$\frac{D_h}{D_j} \simeq \sqrt{\frac{2 + \sqrt{2}}{2 - \sqrt{2}}} \simeq 2.41, \tag{3.6}$$

independent of the jet velocity. From figures 3 and 4 we find $D_h \simeq 10.1$–$10.7\,\text{mm}$, with little apparent dependence on the jet velocity, from which, with $D_j = 4.9\,\text{mm}$, we have $D_h/D_j \simeq 2.1$–2.2 in approximate agreement, to within 9–13%, with this estimate.

In Oğuz *et al.* (1995) it was also shown that the depth Z_0 at which the jet hollow

† Although the derivation used in the reference is correct in principle, the value $\sqrt{3}$ quoted for the numerical constant is in error.

Case	D_c/D_j			L_h/D_j			h/D_j			H/D_j		
	M	E	%	M	E	%	M	E	%	M	E	%
B	4.3	4.5	6	4.6	4.8	4	3.9	4.4	13	8.5	9.2	8
C	4.3	4.8	13	4.9	4.8	2	3.9	4.6	18	8.8	9.4	7
D	4.6	5.3	16	4.7	4.8	2	4.3	4.8	12	9.0	9.6	7
D1	4.9	5.4	10	5.2	5.8	10	4.7	5.3	11	9.9	11.3	12
D2	5.2	5.6	8	4.5	5.3	15	4.3	5.2	7	8.8	10.5	16
D3	5.4	5.6	4	3.4	4.6	26	4.2	4.8	12	7.6	9.4	19
D4	5.0	5.3	6	1.5	3.7	60	2.8	4.2	33	4.3	7.9	45
E	4.9	5.7	18	5.0	4.8	4	4.5	5.0	11	9.5	9.8	3

TABLE 3. Geometrical cavity parameters as defined in figure 6; M denotes measured values, E theoretical values from equations (3.5), (3.8) and (3.9); the column % indicates the percent difference between the two. The bulge is assumed to be spherical in all the cases except D3 and D4, where (3.3) is used.

collapses and pinches off is approximately

$$\frac{Z_0}{D_j} = \frac{1}{4}\left(\frac{D_h}{D_j}\right)^{2/3} Fr^{1/3} \tag{3.7}$$

and the height of the hollow L_h (see figure 6) is related to Fr by

$$\frac{L_h}{D_j} = \frac{1}{2}\left(2\frac{D_h}{D_j}\right)^{2/3} Fr^{1/3}. \tag{3.8}$$

In the present application the distance Z_0 must be measured from the depth of the upper depression estimated in (3.2) above. The depth h of the pinch-off point below the undisturbed pool surface (see figure 6) is thus predicted to be

$$\frac{h}{D_j} \simeq \frac{1}{4}\left(\frac{D_c}{D_j}\right)^{2/3} Fr^{1/3} + 2c(Fr)^{1/4}. \tag{3.9}$$

Estimates based on this formula (with $c = 0.9$) are compared with the data in table 3, where generally they are found to match the observations well.

The volume of the hollow V_c at the moment of pinch-off can be estimated from

$$V_c = \gamma\frac{\pi}{4}(D_h^2 - D_j^2)L_h, \tag{3.10}$$

where γ is about 0.5 according to Oğuz *et al.* (1995). Substitution of (3.6) and (3.8) into this equation yields

$$\frac{V_c}{D_j^3} = c_v Fr^{1/3}, \tag{3.11}$$

where $c_v = (\pi/16)\,m\,(D_h^2/D_j^2 - 1)(2D_h/D_j)^{2/3}$ and m is the ratio of jet velocity at the exit to that at the bottom of the hollow. For cases B to E of table 1, m is approximately equal to 1.3 and, from equation (3.6), $D_h/D_j = 2.41$. Thus we find $c_v \approx 2$.

The heuristic arguments given in this section are based on the assumption of a clear separation in time between the two stages of cavity formation. This is of course an oversimplification that can be expected to hold with greater accuracy for the larger bulges and higher Froude numbers. Indeed, the greatest discrepancies between

estimates and data in table 3 are found for cases D3 and D4 for which $Fr = 33$ and 17 respectively.

We now proceed to describe the results of a more quantitative study of the phenomena observed in this experiment which will further substantiate the qualitative interpretation described in this section.

4. The jet disturbance

The evolution of the bulge depicted in the photos of figure 2 is not only an interesting fluid mechanical phenomenon *per se*, but is also of considerable interest for an understanding of the air entrainment process. For this reason we start with an analysis of this phenomenon that we have conducted with two different models of different level of complexity: a one-dimensional approximation and an axisymmetric boundary-integral formulation. After describing these formulations, we present a comparison of the two predictions between themselves and with experiment.

4.1. *Model*

Our first model for the evolution of the jet disturbance is patterned after that applied by Meier, Klopper & Grabitz (1992), and Meier, Loose & Stasicki (1998) to the similar problem of modulated jets. The starting point is the observation that, if the flow is axisymmetric and the characteristic length of the disturbance large compared with the jet radius, a quasi-one-dimensional model is justified. From figure 2 this assumption would be expected to be good at least in the initial stages of the process. We adopt a cylindrical coordinate system with the polar axis directed downward and write the continuity equation in the form

$$\frac{\partial A}{\partial t} + \frac{\partial}{\partial z}(Au) = 0, \tag{4.1}$$

where $A(z,t)$ is the cross-sectional area of the jet at a distance z below the nozzle exit and $u(z,t)$ is the cross-sectional-averaged vertical velocity positive downward. With the neglect of viscous effects, justified by the relatively high Reynolds number of the flow, the momentum equation may be written, again in the one-dimensional approximation,

$$\frac{\partial u}{\partial t} + u\frac{\partial u}{\partial z} = g - \frac{1}{\rho}\frac{\partial p}{\partial z}. \tag{4.2}$$

Due to the relative thinness of the jet the pressure p can be taken to be uniform over the cross-section and is therefore related to the constant ambient pressure p_0 by

$$p = p_0 + \sigma\mathscr{C}, \tag{4.3}$$

where σ is the surface tension coefficient and the local curvature $\mathscr{C}$ is given by

$$\mathscr{C} = \frac{1 + R'^2 - RR''}{R\left(1 + R'^2\right)^{3/2}}, \tag{4.4}$$

where $R(z,t) = \sqrt{A(z,t)/\pi}$ is the local radius of the jet cross-section and primes denote derivatives with respect to z. Upon non-dimensionalizing the equations in terms of the undisturbed jet velocity U_0 and nozzle diameter D_j, the continuity equation retains the same form (4.1) while the momentum equation (4.2) becomes

$$\frac{\partial u}{\partial t} + u\frac{\partial u}{\partial z} = \frac{1}{Fr} - \frac{1}{We}\frac{\partial \mathscr{C}}{\partial z}. \tag{4.5}$$
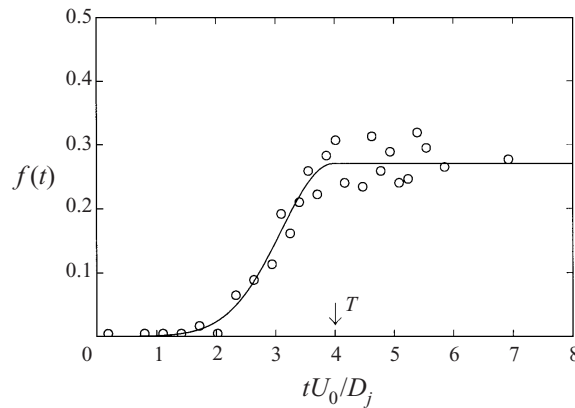
FIGURE 7. Jet exit velocity as a function of time (case D). T is the time necessary for the jet velocity at the exit to reach its maximum value.

Here and in the following we use dimensionless variables although no special notation is adopted.

Equations (4.1) and (4.5) form a hyperbolic system for the solution of which one needs to specify initial and boundary conditions at the jet exit $z = 0$. For the latter we assume

$$A(0,t) = \tfrac{1}{4}\pi, \qquad u(0,t) = 1 + \left(\frac{U_1}{U_0} - 1\right) f(t), \tag{4.6}$$

where $f(0) = 0$ while $f = 1$ for $t \geqslant T$; T is the time necessary for the jet velocity at the nozzle exit to reach its maximum value after the opening of the valves. This valve response function $f(t)$ was measured experimentally by the hydrogen bubble technique. For $0 \leqslant t \leqslant T$ the data were found to be accurately represented by

$$f(t) = \exp\left[-10\left(\frac{t}{T} - 1\right)^2\right]. \tag{4.7}$$

From the measurement T is about 13 ms. An example of how this relation fits the data is shown in figure 7 for case D.

In principle, the initial condition should be found by solving the steady form of (4.1), (4.5) subject to $A(0) = \tfrac{1}{4}\pi$, $u(0) = 1$. For simplicity, however, we assume that the liquid in the jet is in free fall so that

$$u(z,0) = \left(1 + \frac{2z}{Fr}\right)^{1/2}, \tag{4.8}$$

while $A(z,0)$ follows from mass conservation, equation (4.1). We have verified that, since the jet is short, this approximation introduces a negligible error in the solution of the time-dependent problem.

Equations (4.1) and (4.5) are discretized on a uniform staggered grid and solved numerically by the Lax–Wendroff two-stage scheme (see e.g. Fletcher 1988, p. 281). A dimensionless time step $U_0 \Delta t / D_j$ of 0.05 and 200 nodes proved sufficient for a grid-independent solution.

The fifth frame of figure 2 shows that, when the bulge is near the pool surface, its radius has grown too much to justify a quasi-one-dimensional approximation. For this reason, we have complemented the previous calculation by an axisymmetric one
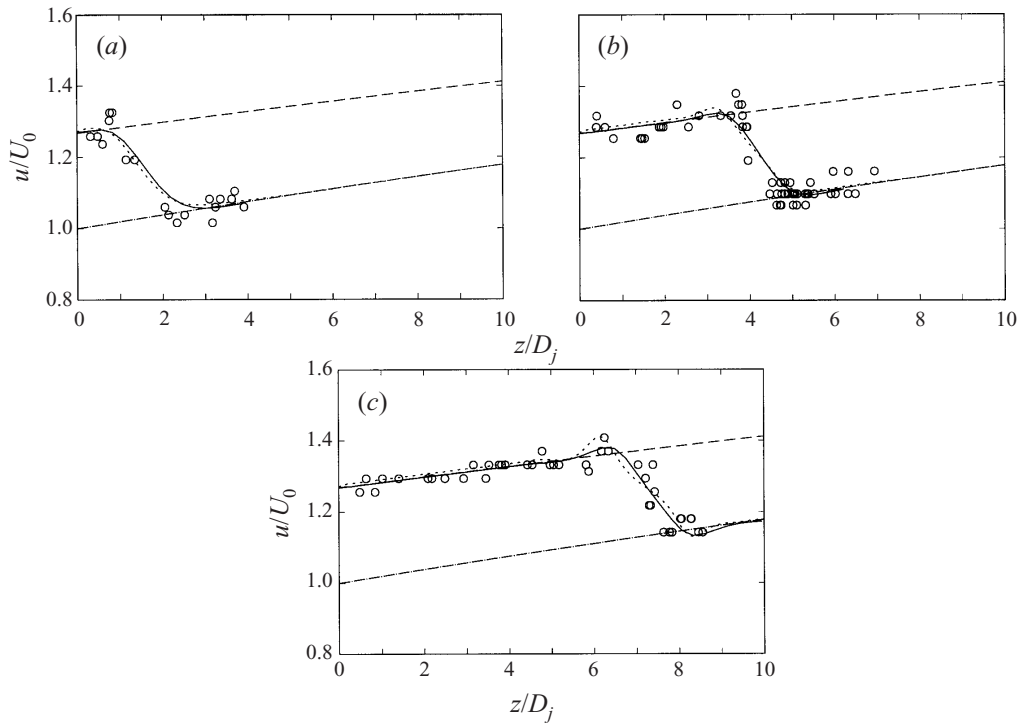
FIGURE 8. Comparison of measured and computed jet velocity distributions at dimensionless times $tU_0/D_j = 4.2$ (*a*), 6.5 (*b*) and 9.0 (*c*). The symbols are the measured data; $\cdots\cdots$, the quasi-one-dimensional simulations ———; the boundary integral simulations; —·—, —— the free-fall velocities (4.8) before and after the opening of the valves.

based on a boundary-integral, potential flow formulation. The numerical method, including the treatment of surface tension, is briefly described in the next section and, in greater detail, in several earlier papers (e.g. Oğuz & Prosperetti 1990; Oğuz *et al.* 1995). The initial conditions and the conditions at the nozzle are the same as in the previous model, i.e. equations (4.6) and (4.8). The velocity distribution in the plane of the nozzle is taken to be uniform.

4.2. *Results*

The two numerical predictions for the liquid velocity in case D at different instants of time are compared with the data in figure 8 as functions of the distance z from the nozzle exit, $z = 0$, to the pool surface, $z/D_j \approx 10.$† The dotted lines are the quasi-one-dimensional results and the solid lines the boundary-integral predictions. The two inclined, approximately straight lines are the free-fall velocity of a jet maintaining the initial undisturbed speed (lower line, dash-and-dots, equation (4.8)), or the final, valves-open speed (upper line, dashed) for all times. It is seen that the two predictions are mostly quite close and only exhibit some difference when the bulge is about to impact the pool surface. The velocity ahead of the bulge follows quite well the lower free-fall line, while that behind the bulge follows the higher free-fall velocity distribution. The two asymptotic states are connected by a transition region which exhibits both overshoots and undershoots with respect to the free-fall lines.

† For the boundary-integral simulation the velocity shown is that at the jet surface; the velocity distribution over the jet cross-section is however essentially uniform.
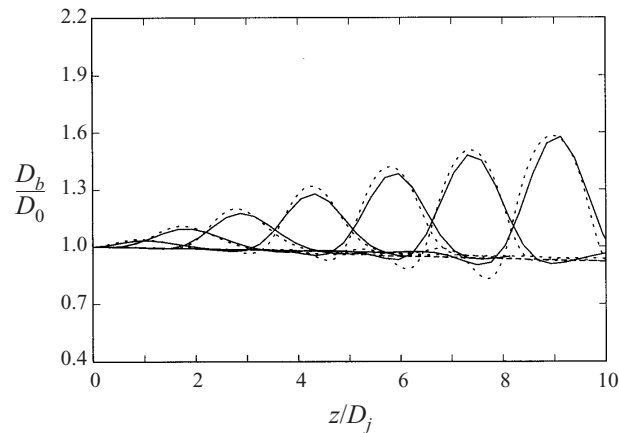
FIGURE 9. Time evolution of the disturbance (case D): ·····, quasi-one-dimensional simulations; ——, boundary-integral method. The dimensionless times tU_0/D_j corresponding to the seven curves are 3.2, 4.2, 5.2, 6.4, 7.7, 9.0 and 10.2, respectively.
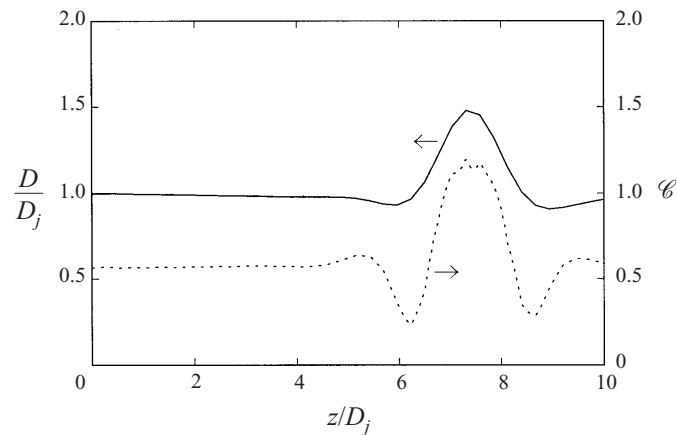

FIGURE 10. Variations of jet diameter (solid line, left scale) and curvature (dashed line, right scale) as a function of z/D_j at $tU_0/D_j = 9.0$ (case D).

Figure 8 also shows the jet velocity data measured by the hydrogen bubble technique. Although there are only a few points within the transition region between the two free-fall velocities, and in spite of some scatter, the measured velocity distributions are in reasonable agreement with the theoretical predictions. In particular, the data seem to support the existence of the under- and overshoots mentioned before.

In addition to the velocity distribution, it is also of interest to present comparisons of the jet shape which we do in figures 9 to 12. Figure 9 compares the jet profile as computed by the quasi-one-dimensional model (dotted line) and the boundary-integral calculation (solid line) at different instants of time, again for case D. The agreement between the two simulations is very good everywhere. The only discernible difference occurs just behind the bulge where the one-dimensional model results in a slightly smaller diameter.

To understand the overshoots and undershoots in the distributions of the jet velocity and diameter around the bulge, we show in figure 10 the local jet diameter (left scale) and the curvature ((4.4), right scale) along the jet for case D at the time $U_0t/D_j = 9$.
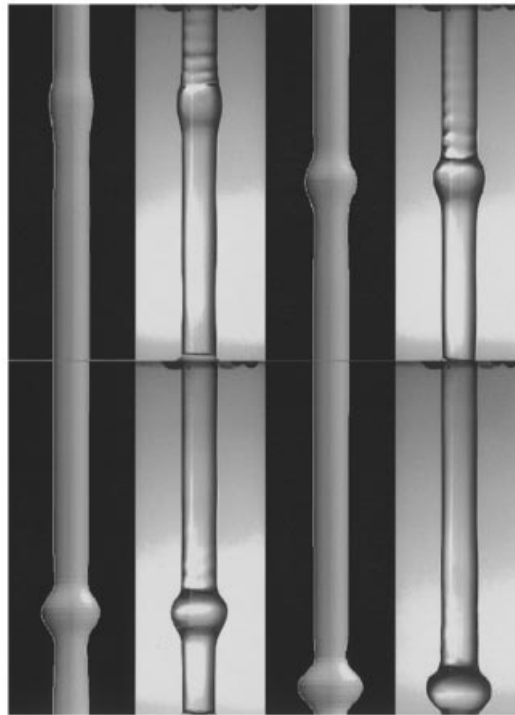
FIGURE 11. Comparison of the calculated and photographed jet profiles at dimensionless times $tU_0/D_j = 2.6$, 4.4, 6.3 and 8.1 for case E.

The bulge is a region of high curvature, corresponding to high pressure, according to equation (4.3), because of the near-stagnation conditions in the free-falling frame of the jet. This region is flanked by two short sections with a smaller radius and higher curvature due to the familiar Rayleigh capillary instability. Between the bulge and these two regions the pressure is small, which accelerates the liquid producing the undershoots and overshoots seen in figure 8. This is the only aspect of the model that is significantly affected by surface tension, which only plays a marginal role in the evolution of the cavity. The situation would be different in the case of a much smaller cavity.

In figure 11 we compare side by side the CCD-camera images with the boundary-integral numerical simulations. The finite-difference results are quite similar, as expected on the basis of figure 9, and are not shown. The only appreciable difference between the two sets of images are the capillary waves trailing the bulge in the photos, which are probably due to oscillations in the system triggered by the abrupt opening of the valves. For example, one may expect that the volume of a few entrapped bubbles inside the nozzle or the tygon tubing will pulsate slightly as a consequence of the sudden exposure to a higher pressure. In any event, these waves are small and they do not seem to have a significant effect on the size and shape of the bulge.

The evolution of the maximum bulge diameter as a function of the distance from the nozzle exit is shown in figure 12 for cases B and D. While the bulge diameter from the one-dimensional model (dotted lines) is slightly greater than that from the boundary integral calculation, the differences are small and both simulations agree with the data to within 8%. A similar agreement was found in the other cases.
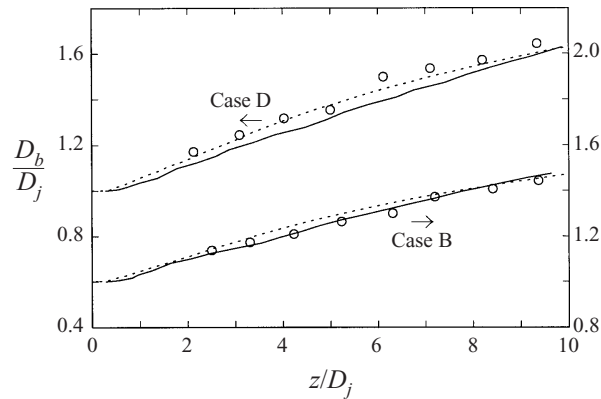
FIGURE 12. Bulge diameter vs. z/D_j for cases B and D. The symbols are the data, the solid line the boundary-integral results, and the dotted line the quasi-one-dimensional model.
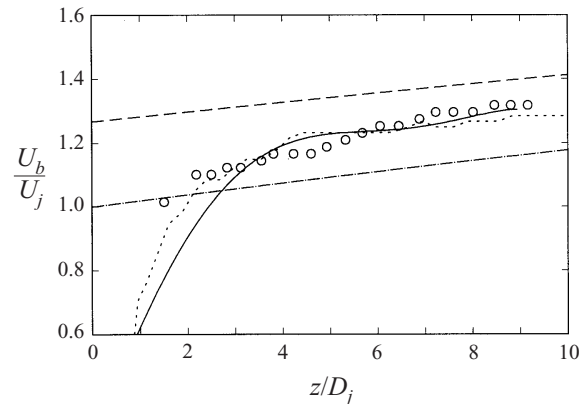

FIGURE 13. Bulge speed as a function of z/D_j for case D. The symbols are the data; $\cdots\cdots$, quasi-one-dimensional simulations; ——, boundary-integral method. The two straight lines are the free-fall velocities as in figure 8.

The computed and measured velocity of propagation of the bulge maximum – i.e. the phase speed – are shown in figure 13 as a function of z for case D. As before, the two inclined lines are the free fall velocities corresponding to open and closed valves. Again one observes a good consistency between the two numerical simulations and a reasonable agreement with the data. Under the action of gravity and of the continuing injection of additional liquid, the phase speed increases always remaining below the higher free-fall velocity line as expected.

5. Boundary-integral method

In the previous section we presented results of a boundary-integral simulation of the evolution of the jet disturbance and in the next section we shall show numerical calculations of the cavity evolution obtained by the same technique. Here we give a short description of the method, referring the reader to our earlier papers (e.g. Oğuz & Prosperetti 1990; Oğuz *et al.* 1995) for more details.

As explained before, prior to the disturbance impact on the pool liquid, the jet

streamlines form a region of separated flow that, being rotational, cannot be simulated by potential flow techniques. For this reason it was necessary to simulate the bulge development and the jet impact separately. This approach is possible because the jet entry into the pool does not affect the upstream conditions appreciably.

Jets can contain an appreciable amount of vorticity depending on the nozzle from which they issue. In our case, however, the rapid and smooth contraction of the nozzle produces a virtually uniform velocity nearly free of vorticity. For the same reason, the rapid increase of jet flow rate when the valves open does not contribute to the production of vorticity. It is therefore justified to treat the development of the jet disturbance by a potential flow model and indeed the good agreement between the numerical results and experiment shown in the previous section substantiates the validity of this approximation.

It has been shown in previous publications that the boundary integral method is also ideally suited to problems involving liquid–liquid impact (Oğuz & Prosperetti 1990) because such flows are highly transient and inertia-dominated. Vorticity remains confined to thin surface layers and has a negligible effect on the flow development. A similar argument applies here as the disruption of the motion of the pool liquid due to the bulge impact is massive and very little dependent on the pre-existing weakly rotational flow conditions.

It is evident from the photos in figures 2–4 that both the bulge development and the jet impact are essentially axisymmetric flows. As indicated in the sketch of figure 6, the computational domain is bounded by a free surface (jet and/or pool) and a fixed boundary (nozzle exit) where a time-dependent, spatially uniform normal velocity is imposed. The assumption of irrotational flow allows us to introduce a velocity potential ϕ which satisfies the Laplace equation. On the jet surface we have the normal stress condition (4.3) as before. By expressing the liquid pressure in terms of the Bernoulli integral and combining it with equation (4.3), the material derivative of ϕ can be written as

$$\frac{\mathrm{D}\phi}{\mathrm{D}t} = \tfrac{1}{2}|\nabla\phi|^2 + \frac{z}{Fr} + \frac{\mathscr{C}}{We}. \tag{5.1}$$

Upon integrating in time, this equation gives the distribution of ϕ on the water surface, which is a Dirichlet boundary condition for the Laplace equation satisfied by the potential. We then write Green's identity for points on the boundaries of the computational domain, i.e. the free surface and the jet exit. A discretization of the integral equation obtained in this way gives a linear algebraic system for the unknowns $\partial\phi/\partial n$ on the free surface and ϕ at the jet exit.

The boundary is discretized by a set of nodes to which cubic splines are fitted. In addition to the coordinates of the nodes, surface parameters such as ϕ, $\partial\phi/\partial z$, $\partial\phi/\partial r$, etc. are also represented by cubic splines. As a rule, a direct boundary-integral method does not allow interpolation schemes higher than piecewise-linear for the unknowns. To be consistent with cubic spline accuracy, we employ an iterative scheme in which corrections of order higher than linear are obtained from the previous iteration. The convergence is typically fast except for surfaces having very high-curvature regions. The added computational effort is justified since this procedure is efficient in terms of increasing the accuracy of the solution. We have used 8 quadrature points between two nodes on the surface in the boundary integrals and the resulting linear system is solved by a standard $L - U$ decomposition technique. As in our previous studies we have adopted an implicit second-order time-integration scheme where the time step is adjusted at each time level to satisfy the stability conditions. To overcome the
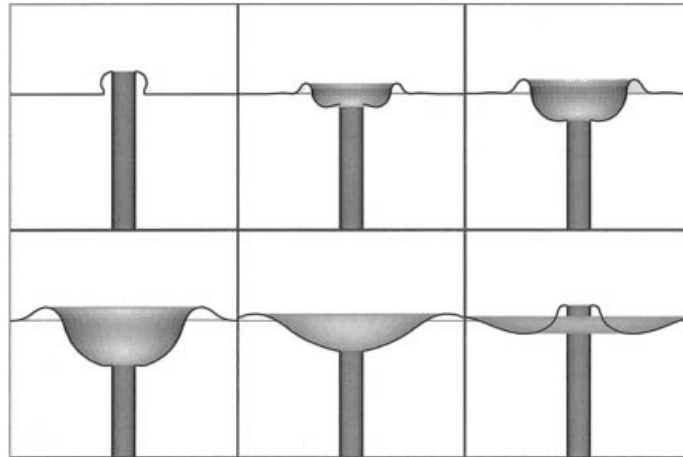
FIGURE 14. Evolution of the free surface of the receiving pool due to the bulge impact only (case C). The dimensionless times tU_0/D_j corresponding to the six images are, from left to right and top to bottom, 0, 2, 4, 12, 18 and 24.

surface instabilities commonly associated with Lagrangian schemes, at every other time step a new set of nodes is generated by taking the midpoints of the old set. In addition, for the other time steps, the nodes are adjusted so as to approximately retain a prescribed spacing. For both operations the cubic spline interpolation of the surface is relied upon. The total number of nodes is adjusted depending on the extent of the free surface so that a consistent resolution is kept throughout the simulation. The free surface is truncated at some large distance from the jet. Convergence tests have shown that this distance needs to be at least 15 jet radii. The bottom of the depression is tracked so that resolution is highest around this region and decreases towards the nozzle exit and the pool surface.

6. The cavity

We now turn to a description of the simulations of the cavity evolution by the boundary-integral technique. In all cases we use as initial condition the bulge shape resulting from the jet disturbance simulation.

Let us suppose first that the cavity is entirely due to the bulge impact while the jet plays a passive role. To model this situation we assume that the jet behaves as a rigid cylinder along which the bulge slides. The results of this simulation are shown in figure 14 for parameter values corresponding to case C. It is seen here that the shape of the cavity at its maximum (fourth frame) is strikingly close to the upper depression shown in the third frame of figure 3. The subsequent evolution found in the experiment is however absent: the depression simply fills up without forming the deeper hollow or entrapping air. This result confirms the validity of the same conclusion reached on the basis of an energy argument in §3. There must be a mechanism by which energy is subtracted from the jet and used to form the cavity.

An upper bound on the jet energy that can contribute to the formation of the cavity is obtained by assuming both the bulge and the jet to impact the free surface, as would happen if the bulge were at the tip of an impacting jet. In this model the presence of the jet ahead of the bulge plays no role. The results of such a calculation with the parameters of case E are compared side-by-side with the photographic images of the
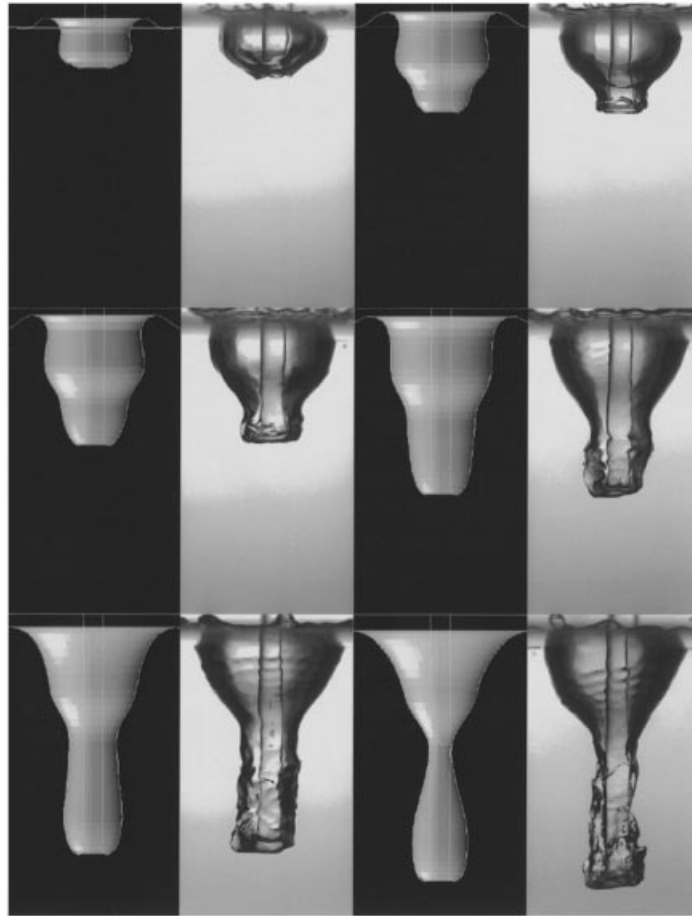
FIGURE 15. Comparison between the observed and computed underwater cavities for case E at dimensionless times $tU_0/D_j = 10.8, 12.7$ (top row), $13.9, 16.4$ (middle row) and $18.8, 20.3$ (bottom row).

cavity in figure 15. A remarkable agreement with the data is observed in spite of the rather extreme approximation of the model.

Figure 16 shows the depth of the cavity below the water surface as a function of the dimensionless time $U_0 t/D_j$ until pinch-off for all the cases of table 1. Different symbols correspond to different pressures in the high-pressure reservoir and, therefore, to different bulge sizes, but with a fixed undisturbed jet exit velocity U_0. All the results are very close, which indicates that the penetration of the cavity front does not depend very much on the disturbance size. This conclusion is in agreement with the picture described earlier in §3 according to which the second stage of the penetration is only dependent on the jet velocity. The lines in figure 16 show the corresponding numerical results in which, as before, the entire jet is assumed to impact the surface. The lines stop at the moment of cavity pinch-off. The bottom of the numerical cavity penetrates deeper than in the experiment and the lines' position below the data indicates that, in the simulation, time runs somewhat slower than in the experiment. The simulation reaches the depth at which pinch-off occurs in the experiment after a time about 15% longer than the measured one. The numerically predicted pinch-off, however, occurs
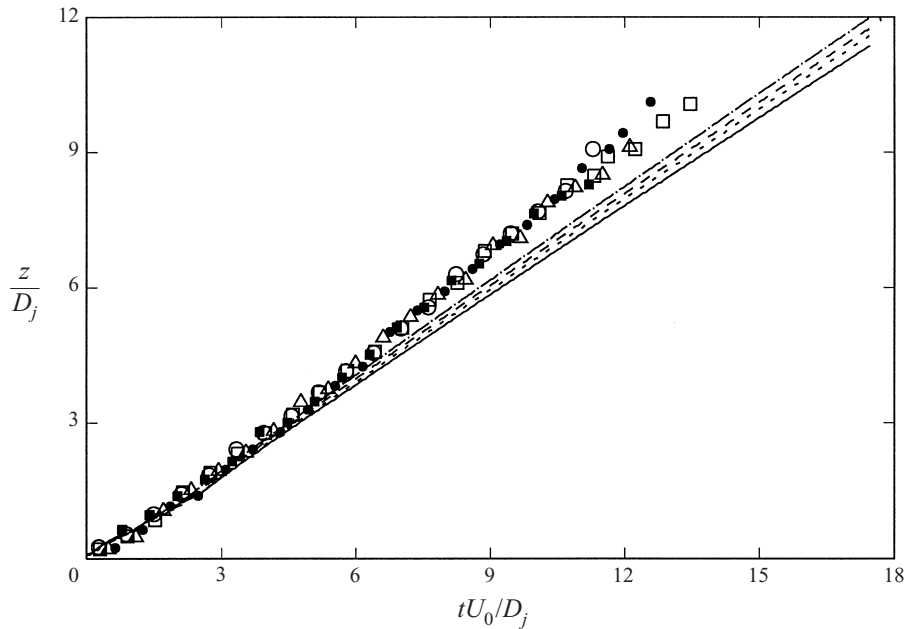
FIGURE 16. Normalized depth z/D_j of the cavity bottom below the undisturbed water level versus time. Symbols show experiments: $\bigcirc$, Case B; $\square$, C; $\triangle$, D; $\bullet$, E; $\blacksquare$, F. Lines show simulations: ———, case B; ·····, C; - - - -, D; —·—, E.

at a greater depth with a time error of about 25%. In view of this difference, in the comparison shown in figure 15, the experimental and computational results are shown at equal values of the actual time divided by the time to pinch-off. In spite of this discrepancy (that, unfortunately, we have not been able to resolve) experiment and simulation are generally in good agreement.

From the measurement of cavity depth versus time, one can calculate the penetration velocity U_c of the cavity front by interpolation and differentiation. Some results are shown in figure 17 as a function of the cavity depth normalized by the jet diameter. The symbols are the experimental results while the lines are the results of the computations for all the cases of table 1. It is a classic result of potential flow theory that, in the absence of gravitational effects, the bottom of the cavity produced by a steady jet advances at a velocity equal to half the jet velocity (see e.g. Birkhoff & Zarantonello 1957). One would expect that, here, the relevant jet velocity would be the free-fall velocity $U_e = \sqrt{U_0^2 + 2gs}$ (where s is the height of the nozzle above the undisturbed pool surface) in the initial stages and $\sqrt{U_1^2 + 2gs}$ later on. One expects therefore that the cavity bottom velocity, normalized by U_e, should be about 0.5 initially, grow to about $\sqrt{U_1^2 + 2gs}/2U_e$ (which, here, ranges between 0.57 and 0.61), and then decline as gravity becomes more important with a deepening of the cavity. The data are in rather precise agreement with these expectations. The computed velocities however are about 10–15% lower than the measured ones as expected in view of the earlier comments in connection with figure 16.

Figure 18 shows the calculated shapes of the cavities just before pinch-off. In addition to the cases shown in table 1, two more cases were computed, one with a large bulge, case G with $U_1/U_0 = 1.5$, and one with no bulge, case H with $U_1/U_0 = 1.0$. The value of D_b/D_j just before striking the surface varies from 1.0 to
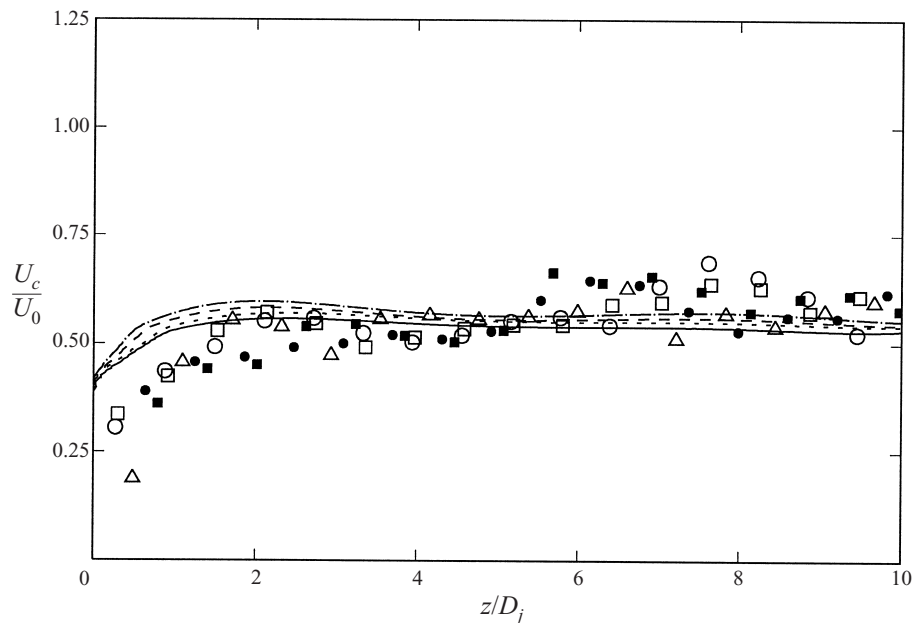
FIGURE 17. Normalized velocity of the cavity bottom U_c/U_e (with $U_e = \sqrt{U_0^2 + 2gs}$) vs. z/D_j. Symbols and lines as in figure 16.

2.10 for the cases shown in the figure. The smaller bulges tend to generate cavities that exhibit a double pinch-off. This feature is the product of the near independence between the depression and hollow dynamics. If the bulge is small, the depression is also small and pinches off at about the same time as the hollow. For larger bulges, the depression's maximum diameter is much greater than that of the hollow and the pinching off occurs either much later (and is therefore not shown in the figure) or not at all. Larger bulges produce a deeper overall cavity size in agreement with equation (3.2). The diameter of the entrapped air cavity is however very little dependent on the bulge size as given by equation (3.6).

The jet model discussed in the previous section points to the effect of the evolution of the bulge as it falls along the jet. To explore this effect we show in figure 19 the cavities computed with jet lengths of 7, 15, and 25 jet diameters as compared with the value of 10 used in the experiment and in the preceding figures. The shape of the bulge at the moment of impact is shown in the first frame for all cases. It should be noted that an increase in jet length also increases the velocity of impact and therefore the Froude number. The ratio between the Froude numbers for the last and the first case is 1.7 so that, according to equation (3.8), the depth of the hollow should increase by 18%, which is in reasonable agreement with the numerical result. Note also that the radius of the cavity increases by 13% according to equation (3.2). This increase is consistent with the numerical simulations.

Another variable of interest is the length of the bulge which, experimentally, could be varied by varying the time scale T. Figure 20 illustrates the difference between a bulge with the length used in the previous simulations (top row) and one twice as long. The longer bulge has more energy and is able to impart a greater impulse to the cavity, so that pinch-off occurs at a slightly later time after the impact. Other than this difference, the two simulations give very similar results.

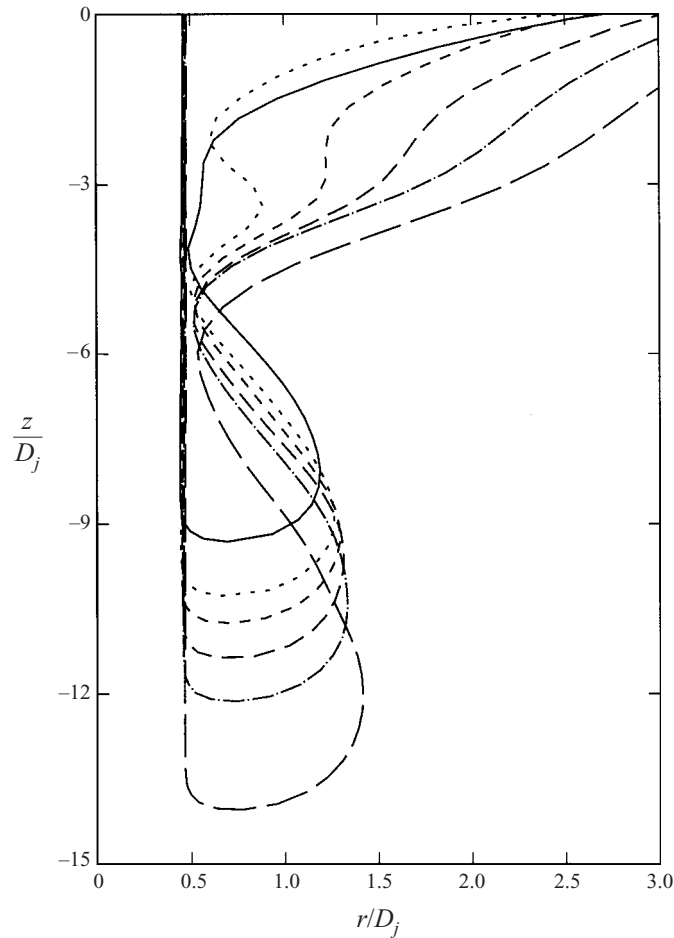Numerical and experimental results for a smaller bulge (case F), obtained by

FIGURE 18. Calculated cavity shapes just before pinch-off; r is the radial distance from the axis of symmetry. In descending order: ——, case H (no bulge); ·····, case A ($U_1/U_0 = 1.05$); ----, case F ($U_1/U_0 = 1.19$); –––, case B ($U_1/U_0 = 1.22$); —·—, case E ($U_1/U_0 = 1.30$); ——, case G ($U_1/U_0 = 1.50$).

reducing the pressure in the high-pressure system, are compared in figure 21. The upper depression is relatively less developed and three-dimensional effects more prominent, but the general phenomenon is essentially the same.

It may be argued that the stagnation pressure due to the bulge impact might be sufficient to deflect the streamlines in the outer layers of the jet, but possibly not near the core. To explore the consequences of such a scenario we have carried out simulations for 'hollow' jets for which only the outer part of the jet impacts the pool liquid, with the core behaving as an undisturbed vertical cylinder (cf. figure 14). Results for $D_{core}/D_j = 0$, 0.5 and 0.7, corresponding to the 100%, 25% and 50% of the full jet flow rate, are shown in figure 22. As the diameter D_{core} of the core of the 'hollow' jet increases, one observes a gradual decrease in the volume, depth, and lifetime of the cavity. One can interpret the phenomenon as corresponding to a smaller 'effective' Froude number. Given the small powers to which Fr is raised in the relations of §3, one expects a gradual effect, in qualitative agreement with the numerical results.
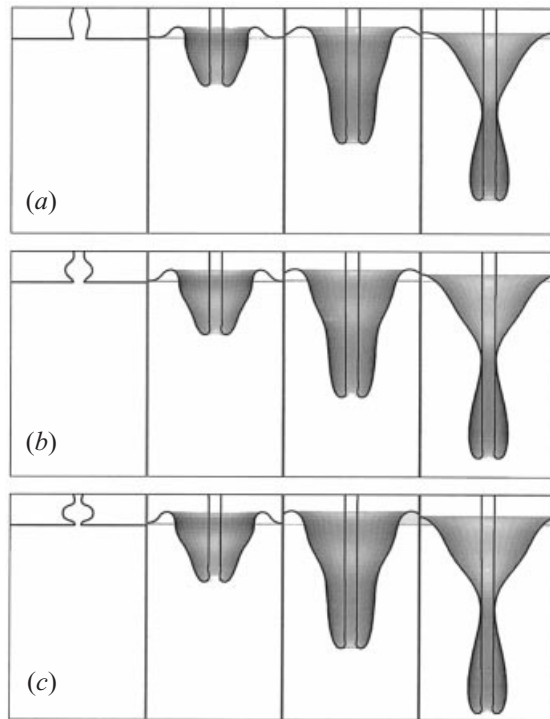
FIGURE 19. Effect of jet length on the development of the bulge and the underwater cavity (case D). (*a*) $L/D_j = 7$; the corresponding times tU_0/D_j are, left to right, 0, 6.4, 12.8 and 19.2; (*b*) $L/D_j = 15$, $tU_0/D_j = 0$, 6.4, 12.7 and 19.1; (*c*) $L/D_j = 25$, $tU_0/D_j = 0$, 6.3, 12.6 and 18.9.
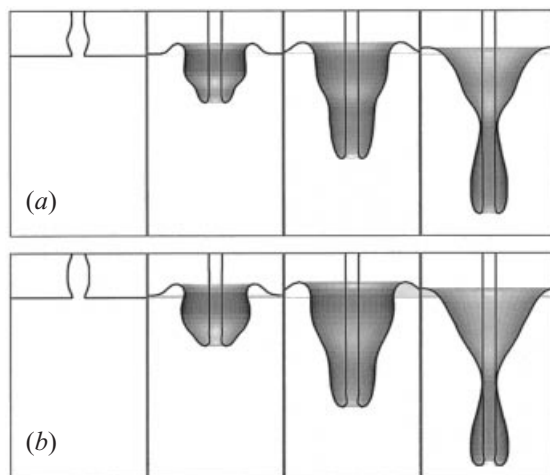

FIGURE 20. Effect of bulge length on the development of underwater cavity (case D). (*a*) $h_b/D_j = 1$; the corresponding times tU_0/D_j are, left to right, 0, 6.4, 12.8 and 19.2; (*b*) $h_b/D_j = 2$, $tU_0/D_j = 0$, 6.5, 13.0 and 19.6.
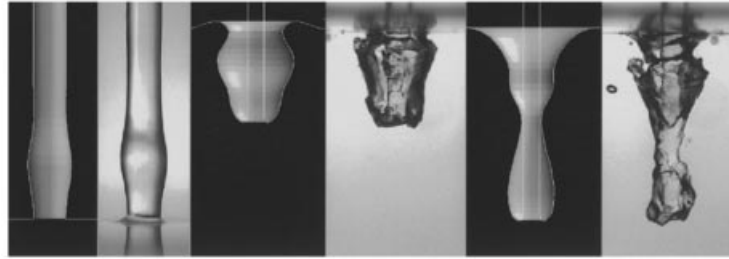
FIGURE 21. Computed and photographed cavity shapes for the case of a small bulge $D_d/D_j = 1.19$ (case F). The dimensionless times tU_0/D_j are 0, 5.2 and 8.9.
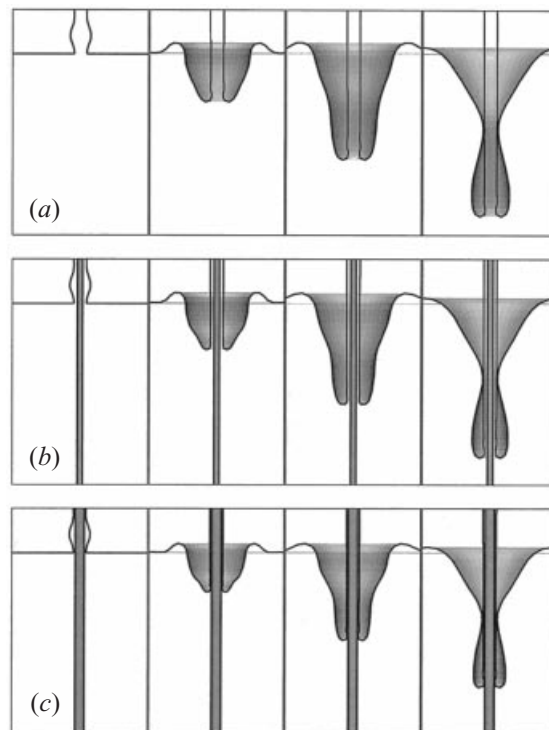

FIGURE 22. Cavity development for different 'hollow' jets (case C). (*a*) $D_{core}/D_j = 0$; the corresponding times tU_0/D_j are 0, 6.1, 12.2 and 18.3; (*b*) $D_{core}/D_j = 0.5$, $tU_0/D_j = 0$, 6.0, 12.1 and 18.1; (*c*) $D_{core}/D_j = 0.7$, $tU_0/D_j = 0$, 5.3, 10.6 and 15.8.

By applying an edge detection technique to the photographic images, a two-dimensional projection of the cavity can be generated. We assume axial symmetry with a local radius given by the average of the two radii that can be measured from these projections. Upon subtracting the volume of the entrapped jet from the total volume of the detached part of the cavity we find the volume of the entrained air. It will be recalled from §3 that this volume should be proportional to $Fr^{1/3}$. All our data are combined in figure 23 where the horizontal axis shows the Froude number and the diameter of the circles is proportional to the bulge size D_b/D_j that ranges between 1.15 and 2.25. The solid line is the prediction (3.11) that is seen to give an
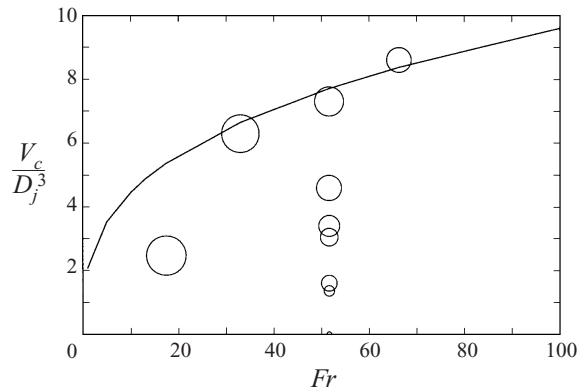
FIGURE 23. Volume of the entrapped air as a function of Froude number. The data are represented by circles with a diameter proportional to the bulge size D_b/D_j which ranges between 1.15 for the smallest circle and 2.25 for the largest. The line is equation (3.11).
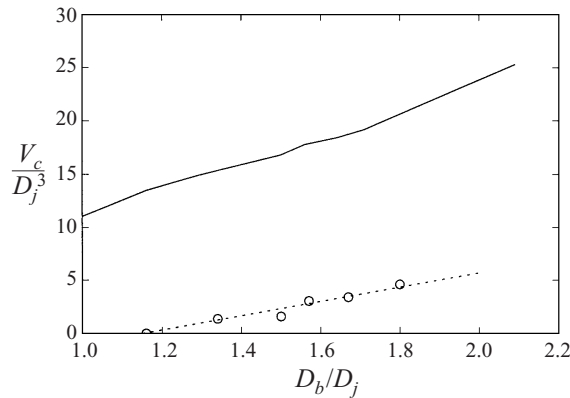

FIGURE 24. Volume of the entrapped air as a function of disturbance size. The circles are the data, the dotted line the fit (6.1), and the solid line the boundary-integral results assuming an impact of the entire jet.

upper limit to the entrained cavity volume as could be expected on the basis of the considerations at the end of § 3.

To better illustrate the dependence on bulge size apparent in figure 23, we show in figure 24 the measured entrained air volumes for the cases of table 1 ($Fr = 52$), as a function of D_b/D_j. In the range covered by the measurements, about $1.16 \leqslant D_b/D_j \leqslant 2.15$, the air volume is approximately linear and closely fitted by the relation

$$\frac{V_c}{D_j^3} = 6.7 \left(\frac{D_b}{D_j} - 1.15 \right), \tag{6.1}$$

which indicates that the jet starts to entrain air only when the bulge size D_b/D_j is larger than about 1.15. For smaller disturbances no entrainment is observed for this jet velocity.

The volume of entrapped air can also be calculated from the simulations. The result of the calculations is shown by the solid line in figure 24. The simulations over-predict the entrapped air by a considerable amount. This conclusion can be ascribed mainly to two features. In the first place, as can be seen e.g. in figures 3

and 4, the process of cavity closure is strongly three-dimensional so that the collapse of the cavity wall onto the jet surface does not occur at the same time all around the jet circumference. The hollow will therefore continue to vent air until the cavity is entirely closed. Secondly, the simulations have been conducted by assuming in all cases that the entire jet impacts, i.e. that the entire jet energy is available for cavity formation. This feature, which explains why air entrainment is predicted even at zero bulge size, is clearly unrealistic as one would expect that the fraction of jet energy available to form the depression is an increasing function of bulge size, at least for the smaller bulges. From the fact noted earlier that there is a good comparison between computed and visualized cavity shape and volume, it would seem that the first factor plays a significantly more important role than the second one.

It is noteworthy that the difference with the data amounts to a nearly constant offset that can reasonably be estimated by calculating the air volume entrapped at zero bulge size, while the slopes of the two lines are very close. From a practical point of view this observation could be interesting although its confirmation requires further study.

7. Conclusions

We have studied the process by which a continuous jet falling onto the free surface of a liquid mass entraps air. We found that, without disturbances, the jet does not entrap air even when its Reynolds and Froude numbers exceed the thresholds reported by earlier investigators. These earlier conclusions were evidently suggested by experimentation with nozzles that, unlike ours, had not been designed to minimize jet turbulence.

We have found that, in order to entrain air, it is necessary to introduce artificial disturbances. This we do in a reproducible and controlled manner by a rapid increase of the jet flow rate. The jet disturbance thus generated interacts in a complex way with the jet itself and leads to the development of a relatively large air cavity the bottom part of which pinches off giving rise to air bubbles. For a given jet velocity, the volume of entrapped air is found to be approximately proportional to the characteristic size of the jet disturbance.

The series of complex phenomena observed in the experiment can be explained qualitatively on the basis of a simple model in which the depression produced by the disturbance is essentially decoupled from the subsequent hollow that, due to the jet, forms at its bottom. A more quantitative theoretical analysis by numerical means produces results that are in good agreement with observation until the closure of the air cavity.

REFERENCES

Bín, A. K. 1993 Gas entrainment by plunging liquid jets. *Chem. Engng Sci.* **48**, 3585–3630.

Birkhoff, G. & Zarantonello, E. H. 1957 *Jets, Wakes, and Cavities.* Academic.

Bonetto, F. & Lahey, R. T. 1993 An experimental study on air carryunder due to a plunging liquid jet. *Intl J. Multiphase Flow* **19**, 281–294.

Detsch, R. M. & Sharma, R. N. 1990 The critical angle for gas bubble entrainment by plunging liguid jets. *Chem. Engng J.* **44**, 157–166.

Ervine, D. A., McKeogh, E. & Elsawy, E. M. 1980 Effect of turbulence intensity on the rate of air entrainment by plunging water jets. *Proc. Inst. Chem. Engrs* **69**, 425–445.

Fletcher, C. A. J. 1988 *Computational Techniques for Fluid Dynamics.* Springer.

Funatsu, K., Hsu, Y. & Kamogawa, T. 1988 Gas holdup and gas entrainment of a plunging water jet with a constant entrainment guide. *Can. J. Chem. Engng* **66**, 19–28.

Gilbarg, D. & Anderson, R. A. 1948 Influence of atmospheric pressure on the phenomena accompanying the entry of spheres into water. *J. App. Phys.* **19**, 127–139.

Kusabiraki, D., Niki, H., Yamagiwa, K. & Ohkawa, A. 1990 Gas entrainment rate and flow patterns of vertical plunging liquid jets. *Can. J. Chem. Engng* **68**, 893–903.

Lara, P. 1979 Onset of air entrainment for a water jet impinging vertically on a water surface. *Chem. Engng Sci.* **34**, 1164–1165.

Lin, T. J. & Donnelly, H. G. 1969 Gas bubble entrainment by plunging laminar liquid jets. *AIChE J.* **12**, 563–571.

McKeogh, E. J. & Elsawy, E. M. 1980 Air retained in pool by plunging water jet. *ASCE J. Hydraul. Div.* **106**, 1577–1593.

Meier, G. E. A., Klopper, A. & Grabitz, G. 1992 The influence of kinematic waves on jet break down. *Expts. Fluids* **12**, 173–180.

Meier, G., Loose, S. & Stasicki, B. 1998 Unsteady liquid jets. *Appl. Sci. Res.* **58**, 207–216.

Oğuz, H. N. & Prosperetti, A. 1990 Bubble entrainment by the impact of drops on liquid surfaces. *J. Fluid Mech.* **219**, 143–179.

Oğuz, H. N., Prosperetti, A. & Kolaini, A. R. 1995 Air entrapment by a falling water mass. *J. Fluid Mech.* **294**, 181–207.

Ohkawa, A., Kusabiraki, D. & Sakai, N. 1987 Effect of nozzle length on gas entrainment characteristics of vertical liquid jet. *J. Chem. Engng Japan* **20**, 295–300.

Prosperetti, A. & Oğuz, H. 1993 The impact of drops on liquid surfaces and the underwater noise of rain. *Ann. Rev. Fluid Mech.* **25**, 577–602.

Richardson, E. G. 1948 The impact of a solid on a liquid surface. *Proc. Phys. Soc.* **61**, 352–367.

Sene, K. J. 1988 Air entrainment by plunging jets. *Chem. Engng Sci.* **43**, 2615–2623.

Van de Sande, E. & Smith, J. M. 1976 Jet break-up and air entrainment by low velocity turbulent water jets. *Chem. Engng Sci.* **31**, 219–224.

Worthington, A. M. 1908 *A Study of Spalshes.* Longmans Green and Company, New York.